Atmos. Meas. Tech. Discuss., 7, 4481–4528, 2014
www.atmos-meas-tech-discuss.net/7/4481/2014/
doi:10.5194/amtd-7-4481-2014


Atmospheric Measurement Techniques
Open Access
Discussions



# New algorithm for integration between wireless microwave sensor network and radar for improved rainfall measurement and mapping

**Y. Liberman**[1], **R. Samuels**[2], **P. Alpert**[2], **and H. Messer**[1]

[1]Tel Aviv University, School Of Electrical-Engineering, Tel Aviv 6997801, Israel
[2]Tel Aviv University, Porter School for environmental studies, Tel Aviv 6997801, Israel

Received: 28 December 2013 – Accepted: 5 April 2014 – Published: 6 May 2014

Correspondence to: Y. Liberman (yoavliberman@mail.tau.ac.il)

Published by Copernicus Publications on behalf of the European Geosciences Union.

## Abstract

One of the main challenges for meteorological and hydrological modelling is accurate rainfall measurement and mapping across time and space. To date the most effective methods for large scale rainfall estimates are radar, satellites, and more recently, received signal level (RSL) measurements received from commercial microwave networks (CMN). While these methods provide improved spatial resolution over traditional rain gauges, these have their limitations as well. For example, the wireless CMN, which are comprised of microwave links (ML), are dependant upon existing infrastructure, and the ML arbitrary distribution in space. Radar, on the other hand, is known in its limitation in accurately estimating rainfall in urban regions, clutter areas and distant locations. In this paper the pros and cons of the radar and ML methods are considered in order to develop a new algorithm for improving rain fall measurement and mapping, which is based on data fusion of the different sources. The integration is based on an optimal weighted average of the two data sets, taking into account location, number of links, rainfall intensity and time step. Our results indicate that by using the proposed new method we not only generate a more accurate 2-D rainfall reconstructions, compared with actual rain intensities in space, but also the reconstructed maps are extended to the maximum coverage area. By inspecting three significant rain events, we show an improvement of rain rate estimation over CMN or radar alone, almost uniformly, both for instantaneous spatial measurements, as well as in calculating total accumulated rainfall. These new improved 2-D rainfall maps, and the accurate rainfall measurements over large areas at sub-hourly time scales, will allow for improved understanding, initialization and calibration of hydrological and meteorological models necessary, mainly, for water resource management and planning.





AMTD
7, 4481–4528, 2014

## 1 Introduction

The need for reliable, high resolution rainfall measurement and mapping is increasing, as such data are the principle drivers for hydro-meteorological models, climate studies, urban planning and flood warning systems. Current methods including rain gauge, radar, ML, and even satellites, can provide measurements, yet the ability to generate high resolution maps from them is limited. Rain gauges, which provide the most reliable estimates, are limited due to their point location measurements which cannot provide accurate spatial estimates, especially in areas of complex topography or high spatial variability. Other methods, which have been adopted to overcome this spatial challenge, include radar estimates, and more recently, measurements from wireless microwave link networks (Messer et al., 2006). Naturally, due to both environment and technological limitations, the estimates from such sources may have high levels of uncertainty and errors (e.g., Mackenzie et al., 1993). For meteorologists and hydrologists attempting to use this information either to better understand storm dynamics, on one hand, or to inform infrastructure planning on the other, each of these methods has unique information. Given this plethora of data, it has recently been acknowledged that precipitation estimates with a spatial and temporal resolution of 4 km and 30 min, respectively, are realistic target levels useful for many researches and applications, (Sorooshian et al., 2011). This is particularly true for estimation of orographic rainfall distribution on the high meso-gamma scale resolution, as reviewed by Alpert et al. (1994). Unfortunately, the formats of the data, as well as the varying scales and limitation on their availability make it difficult to use them in a complementary way.

In this paper we present a new technique for integrating between radar and CMN data in order to improve the accuracy and reliability of rainfall estimates. The integration of multiple sources allows for weighing the estimates appropriately in-line with the advantages and disadvantages of the multiple rain sources included. This design leaves room for the incorporation of other data sources (i.e., satellite data) in the future.

Furthermore, this paper also demonstrate how the integrative approach provides better instantaneous as well as cumulative rainfall estimates, both spatially and temporally, when compared with rain gauge measurements over the same area. Specifically, we analyze three intense rain events which occurred over Israel in January 2010, January 2013 and December 2009.

This paper is organized as follows: Sects. 1.1 and 1.2 describe the different measurement sources used in this paper. Section 1.3 covers the study area and details surrounding of the chosen rain events. In Sect. 2 we provide full description of the novel integrative approach. This is followed by results of the analysis and conclusions regarding the application and future development of such an important integrative tool, as detailed in Sect. 3. We conclude this paper in Sect. 4.

### 1.1 The weather radar

Over the past half century, starting in the late 1940's, the use of radar for estimating rainfall measurements was proposed by Marshall et al. (1947). The well known empirical relationship between the radar reflectivity and the rainfall intensity is shown in Eq. (1):

$$Z = ar^b \tag{1}$$

Where $r$ is the rain rate (in $\mathrm{mm\,h^{-1}}$), $Z$ is the radar reflectivity (in $\mathrm{mm^6\,m^{-3}}$), and $a$, $b$ are known constants, mainly, a function of the drop size distribution (DSD). These parameters may vary according to different rain types both between and within storms, which can lead to high levels of error and uncertainty in the radar, as detailed in Morin et al. (2003). Additional sources of the radar uncertainty (Germann et al., 2006), include: attenuation at C and X-band, bright band contamination, and clutter regions.

Additionally, the spatial expansion effect of the radar beam results in an increase of the reflective volume up to a few kilometres which may lead to partial beam filling; this, in turn, may result in overestimation of rain rates. Additionally, radar measurements





AMTD
7, 4481–4528, 2014

aloft are uncertain estimates of near-ground rainfall due to ground clutter, changes of Drop Size Distribution (DSD) as a function of height due to evaporation, coalescence, raindrop collection and breakup (Prat and Barros, 2009) In order to deal with these uncertainties, different approaches have been proposed including the use of a Polarimetric or Doppler weather radars (e.g., Bringi and Chandrasekar, 2001; Doviak et al., 1979). Such systems use the shape of the rain drops and allow for improvement of rain rate estimation (Meischner et al., 1991).

Another limiting factor in the radar accuracy is the location of the radar. The received signal can provide reasonable rainfall estimation for up to around 100 km, though this is also dependent upon topography and the height of the radar beam. Thus, for objects too close to the radar (i.e., < 1 km), or too far away (i.e., > 100 km), reconstruction is characterized by much uncertainty. In the case where the distance is greater than 150 km, no estimation can be provided by radar. In other words, the weather radar inaccuracy increases as the distance to the area grows (with respect to $R^2$). This fact can also be derived from the radar equation as follows (Skolnik, 1962):

$$P_r = P_t \tau G^2 \lambda^2 \theta^2 \frac{c}{512\pi^2} \frac{\eta}{R^2} \propto \frac{\text{Const}}{R^2} \quad (2)$$

Where $P_r$ is the received power, $P_t$ is the transmitted power, $G$ is the gain of the transmitting antenna, $\lambda$ is the radar wavelength, $\eta$ (in dB km), is the Radar Cross Section – RCS of the target area, (Mackenzie et al., 1993). $R$ is the distance from the transmitter to the target area. One can see that the more distant the area (target) is from the radar, the lower the received signal (denoted as $P_r$) is, hence the inaccuracy increases.

## 1.2 Microwave Links – ML

A wireless microwave signal's strength, also known as RSL (received signal level), is majorly affected by precipitation (mainly rain). The well-known empirical attenuation-rain rate relation is given by Olsen (1978):

$$A = \alpha R^{\beta} L \quad (3)$$





AMTD
7, 4481–4528, 2014

where $A$ (expressed in dB) is the measured RSL, $R$ (expressed in mm h$^{-1}$) is the path averaged rain rate (along the ML), $L$ (expressed in km) is the link length, and $\alpha$, $\beta$ are constants, depending mainly on the link frequency and the drop size distribution (DSD), as detailed in Örs et al. (1999). The RSL is measured by a variety of antennas distributed in space (e.g., see Fig. 1), with typical frequencies of 18–23 GHz, and lengths that vary between 1–20 km. The measurements are given in pre-set temporal resolution, with known quantization level. Because we are trying to reconstruct rain fields, we inspect only significant rain events, thus, we may assume that our RSL has very high signal-to-noise ratio (SNR). A typical such RSL is shown in Fig. 2. In the figure, the RSL is provided with magnitude resolution of 0.1 dB, at 15 min sampling rate, for a link located in the center of Israel (between Ramle and Hasmonaim, provided by – Cellcom ltd.). In order to overcome non-linearities, the RSL is presented after a pre-processing stage, as detailed in the M.Sc. thesis of Liberman (2013).

Since the use of commercial ML for rainfall monitoring was first suggested by Messer et al. (2006), multiple methodologies for rainfall estimation and mapping have been suggested (e.g., Goldshtein et al., 2009; Overeem et al., 2013). Furthermore, precipitation monitoring in general and rainfall monitoring in particular is a subject of interest by many researchers all around the world since 2006 to this day (e.g., Chwala et al., 2012; Overeem et al., 2011). In this paper, a novel algorithm which has been recently developed for recovering rainfall maps using RSL measurements. The basis of this algorithm is described here, more details can be found in Liberman (2013).

For any given set of RSL measurements from ML, the goal is to construct the most accurate approximation of the rain rate along the links, and then to reconstruct the rain field in the links' vicinity. Suppose we have a set of observed rainfall-induced RSL attenuations from $M$ ML in a given geometry (denoted as $A_j$, for $j = 1,\ldots,M$). It was offered to modify Eq. (3), so that each link's RSL can be written as:

$$A_j = \alpha_j R_j^{\beta_j} L_j = \int_{L_j} \alpha_j r^{\beta_j}(x)\mathrm{d}x \tag{4}$$

where $r(x)$ (expressed in $\mathrm{mm\,h^{-1}}$) is the true instantaneous rain rate at a point $x$ along the link, $L_j$ (expressed in km) is the $j_{th}$ link length and $\alpha_j$, $\beta_j$ are the known $j$th link constant parameters (as described in Örs et al., 1999). Now, by dividing each link into $n_j$ (small enough) equal segments, we may approximate the integral in Eq. (4) and derive the following non-linear relation between each link's RSL and the actual rain rate along it (i.e., along an arbitrary "line" in space):

$$A_j \approx \alpha_j \sum_{i=1}^{n_j} r_{ij}^{\beta_j} l_{ij} \tag{5}$$

Where $l_{ij}$ is the length of the $i$th segment (for each $j$th link), and $r_{ij}$ is the unknown rain rate in each $l_{ij}$ segment, where $l_{ij}$ is subject to: $l_{ij} \ll L_j$.

A unique and optimal solution can be found for Eq. (5). A rain field is generally represented in a sparse manner, as has been observed by many in the literature (e.g., Morin et al., 2006). This means that for some extent of the rain field, it is reasonable to assume that the rain field is mostly depicted in a sparse manner, thus, we can assume that the solution for each $r_{ij}$ (denoted as the rain rate for each $j$th link in each $i$th segment where the ML are available) is mostly sparse. Therefore, the optimization "$L_1$ problem" (as discussed in Chen et al., 1998) can be solved. Moreover, it can be proved that the solution is unique and optimal if some regularity conditions, mainly regarding the links distribution in space and the derived solution to the $L_1$ Problem, are satisfied.

The next step is to construct a 2-D rain field map from the estimated solution of Eq. (5). That could be achieved by using either parametric, or non-parametric interpolation methods.

### 1.3 Available data and coverage area

The coverage area of the radar includes all the coordinates in space that lie between $0.1 \leq R_i \leq 150\,\mathrm{km}$ from the radar location, where $R_i$ indicates the radar radius distance from each $[x_i,\ y_i]$ coordinate. In this study, the data from the weather radar, which is located in Bet Dagan (32.007° N, 34.814° E), is provided by the Israel Meteorological





AMTD
7, 4481–4528, 2014

Service (IMS – see Fig. 1). The measurements from the radar are provided at a resolution of 1 km$^2$ every 5 min. Though the employed radar in Israel has an "automatic clutter removal" (Skolnik, 1962), dominant clutter can still be observed in the north of Israel, where many hilled areas are found (e.g., in Ramat HaGolan: 32.58° N, 35.44° E).

Regarding the ML, we define the covered areas dependent upon the location of the specific microwave links. Here, operational microwave link data for the center-south of Israel was provided by Cellcom ltd. (i.e., 96 operating microwave links) and Pelephone ltd. (30 operating microwave links), as shown in Fig. 1. The ML operate at frequencies of 18–23 GHz and are horizontally or vertically polarized, with lengths that range from 3–20 km and with magnitude resolutions of 0.1 db for Cellcom ltd. and 1 db for Pelephone, which may cause a degradation in the accuracy of the estimated rainfall using ML, but because in this study we analyzed only heavy rain events (high SNR data, Sect. 1.2), the effect of the magnitude resolution on the reconstruction accuracy is negligible. Also, 15 min minimum and maximum RSL values were provided by Cellcom ltd. and 1 min temporal resolution was provided by Pelephone ltd. In this study, three major set of rain events were chosen for the analysis: *Event (1)*, 18–19 January 2010 (24 h of rain). *Event (2)*, 7–10 January 2013 (96 h of rain). *Event (3)*, 30 December 2009 (24 h of rain).

Rainfall estimates from the set of events (1), (2) and (3) are validated against a network of 70 tipping bucket rain-gauges distributed throughout the region (as demonstrated in Fig. 3) recording at a time resolution of 10 min, where each rain gauge provides ground truth (accumulated) rain measurements in mm, which is equivalent to water volume per m$^2$.

## 2 The integrative approach

In this section, we fully detail the integration procedure, whose main goal is to combine the different rainfall measurements in a way which optimally weighs the advantages and disadvantages of the various methods. As mentioned above, the radar data are





AMTD
7, 4481–4528, 2014

provided by the IMS, while the RSL data are provided by Cellcom ltd. and Pelephone cellular companies.

Data assimilation is widely used in many environmental fields, in particular in weather modelling (e.g., Chahine et al., 2006) and in hydrological modelling (e.g., McLaughlin, 2002). In data assimilation, we are required to form a relationship between the state we want to estimate (e.g., the 2-D distribution of rainfall intensity) to the different observation sources (e.g., Radar and ML). We can assume that the process relationship between the observations and the desired estimate is represented by a forward model (denoted as $f$), which is defined in Eq. (6):

$$R_{\mathrm{int}}(x_i, y_i) = f(R_{\mathrm{rad};i}, R_{\mathrm{ml};i}) \tag{6}$$

where $R_{\mathrm{int}}(x_i, y_i)$ is the required state (rainfall intensity, in each $x_i, y_i$ coordinates in space, $R_{\mathrm{rad};i}$ and $R_{\mathrm{ml};i}$ are the rainfall intensities achieved by the radar and the ML observations, respectively, for each $x_i, y_i$ coordinate in space (where the data is available). Fig. 1 shows the study area where data from either or both radar and ML are available (i.e., in the case of the ML, we divided the space into areas of interest). In order to generate the most reliable reconstruction of rainfall maps, we define the following rules, based on the characteristics of the different measurement sources:

1. For all the coordinates which are not covered by ML (i.e., the coordinates where the reconstruction by the ML is not available, e.g. in Fig. 1), we *only regard the reconstruction received by the radar*, if available. That is, for any $[x_i, y_i]$ coordinate, which is not covered by the ML but satisfies: $0.1 \le R_i \le 150$.

2. Inside an area of interest, where ML are found, we check if both the following regular conditions are satisfied:

   a. The distribution of the links in space satisfy the reconstruction ability condition, as discussed and proved in Sendik and Messer (2012), providing enough data so that a highly reliable reconstruction is possible along the links in an area of interest.

b. The estimated rain intensity coordinates in space along the links (which are distributed in an arbitrary manner in space) satisfy the generalized Shannon–Nyquist sampling Theorem for non-uniform sampling, as detailed in Eldar (2003).

3. If Condition 1 and Condition 2 are not satisfied inside an area of interest, we apply a new weighted algorithm, using both of the sources in the study area. The rainfall measurement will then rely *both* on the links distribution in space and the radar radius, as shown in Eq. (2).

If both of the conditions stated above are satisfied in a given area, an optimal recovery of the rainfall, using ML, in that area is possible (Liberman, 2013). Hence, *we do not consider the radar reconstruction in that area at all*. If Condition 3 is satisfied, we require some sort of integration scheme between the ML and the radar. For this integration we propose a weighted linear model, mainly due to the fact that in previous data assimilation works, especially for hydrological and weather forecasts, linear models were adopted and proven useful (e.g., Daley, 1993).

It should be noted that before the integration is applied, both the radar and the ML data undergo some preprocessing stage. For example, dominant clutter areas (denoted as Clutter), which are characterised by much uncertainty in the radar reconstruction (see Sect. 1.3), are determined by using prior information and rain gauges measurementes. Regarding the ML RSL data, a zero level reduction, noise removal and other preprocessing schemes are applied before the rainfall maps are created, as further detailed in Liberman (2013). Hence, by using the proposed conditions above, we may rewrite $R_{\text{int}}$ in Eq. (6) as shown in Eq. (7):

$$R_{\text{int}}(x_i, y_i) = \begin{cases} R_{\text{rad};i}, \ 0.1\,\text{km} \le R_i \le 150\,\text{km} \cap N_i = 0 \\ R_{\text{ml};i}, \ N_i > 1 \cap (R_i \ge 150\,\text{km} \cup R_i \le 0.1\,\text{km} \cup \text{Condition 2} \cup \text{Clutter}) \\ f_{\text{Lin}}(R_{\text{ml};i}, R_{\text{rad};i}), \ N_i > 0 \cap 0.1\,\text{km} \le R_i \le 150\,\text{km} \cap \text{No Clutter} \end{cases} \tag{7}$$





AMTD
7, 4481–4528, 2014

Where in Eq. (7): $R_{\mathrm{rad};i}$ and $R_{\mathrm{ml};i}$ are the rain rate values, in the $[x_i, y_i]$ coordinates, for the Radar and ML, respectively. $N_i$ indicates the number of links in the area of interest, for which the $[x_i, y_i]$ coordinate belongs to. $R_i$ is the distance (denoted as the Radar radius, expressed in km) between the radar location and each $[x_i, y_i]$ coordinate in space. $\cup$ and $\cap$ indicate the *Or* and *And* operators, respectively. $f_{\mathrm{Lin}}$ is a linear function of $R_{\mathrm{ml};i}$ and $R_{\mathrm{rad};i}$, which is defined by:

$$f_{\mathrm{Lin}}(R_{\mathrm{ml};i}, R_{\mathrm{rad};i}) = \tilde{\alpha}_{\mathrm{rad};i} R_{\mathrm{rad};i} + \tilde{\alpha}_{\mathrm{ml};i} R_{\mathrm{ml};i} \tag{8}$$

where $f_{\mathrm{Lin}}$ is calculated in each $[x_i, y_i]$ "common" coordinates (i.e., where rain intensities are provided both by the Radar and ML) in space. $\tilde{\alpha}_{\mathrm{rad};i}, \tilde{\alpha}_{\mathrm{ml};i}$ denote the *normalized* Radar and ML weights, respectively. These weights are a function of the radar radius (denoted as $R_i$) and the number of links in the area of interest (denoted as $N_i$), in each $[x_i, y_i]$ common coordinates (i.e., where Condition 3 is satisfied). Since $\tilde{\alpha}_{\mathrm{rad};i}, \tilde{\alpha}_{\mathrm{ml};i}$ are subject to $\tilde{\alpha}_{\mathrm{rad}} + \tilde{\alpha}_{\mathrm{ml}} = 1$, we may model these weights as follows:

$$\tilde{\alpha}_{\mathrm{rad};i} = \frac{\alpha_{\mathrm{rad}}}{\alpha_{\mathrm{rad}} + \alpha_{\mathrm{ml}}} \tag{9a}$$

$$\tilde{\alpha}_{\mathrm{ml};i} = \frac{\alpha_{\mathrm{ml}}}{\alpha_{\mathrm{rad}} + \alpha_{\mathrm{ml}}} \tag{9b}$$

Where $\alpha_{\mathrm{rad}}, \alpha_{\mathrm{ml}}$ are denoted as the Radar and ML, *non normalized*, weights, respectively. From Eq. (9), it is clear that $\tilde{\alpha}_{\mathrm{ml}} + \tilde{\alpha}_{\mathrm{rad}} = 1$, hence, this offered model is valid. As mentioned before, the accuracy in the reconstruction of rain fields, derived by the radar and the ML, is dependent, mainly, on the number of links and the radar radius (distance from the target area) in each coordinate. Thus, for each $[x_i, y_i]$ coordinate, which satisfies Condition 3, we offer to model $\alpha_{\mathrm{ml}}$ and $\alpha_{\mathrm{rad}}$ as follows:

$$\alpha_{\mathrm{rad}} = \frac{c_\mathrm{r}^2}{c_\mathrm{r}^2 + R_i^2} \tag{10a}$$

$$\alpha_{\mathrm{ml}} = \frac{N_i^2}{N_i^2 + c_\mathrm{l}^2} \tag{10b}$$

Where in Eq. (10a) and Eq. (10b), $c_\mathrm{r}$ and $c_\mathrm{l}$ are the radar and ML weight constants, respectively. From the definition of the weights in Eq. (10), it is clear that as $N_i$ is higher, $\tilde{\alpha}_{\mathrm{ml};i}$ is higher, and accordingly, as $R_i$ is lower (closer to the radar location), $\tilde{\alpha}_{\mathrm{rad};i}$ is higher, thus, it is the natural choice of the weights. It should be noted that other forms of weights (e.g., exponential weights) were also considered for the integration, which proved to be less accurate than the ones proposed here. Future work may focus on other forms of weights for the integration. Now, by substituting Eq. (10a) into Eq. (9a), and Eq. (10b) into Eq. (9b), we derive the following relation:

$$\tilde{\alpha}_{\mathrm{rad};i} = \frac{(N_i^2 + c_\mathrm{l}^2)c_\mathrm{r}^2}{(N_i^2 + c_\mathrm{l}^2)c_\mathrm{r}^2 + (c_\mathrm{r}^2 + R_i^2)N_i^2} = h_i(c_\mathrm{l}, c_\mathrm{r}) \tag{11a}$$

$$\tilde{\alpha}_{\mathrm{ml};i} = \frac{(c_\mathrm{r}^2 + R_i^2)N_i^2}{(N_i^2 + c_\mathrm{l}^2)c_\mathrm{r}^2 + (c_\mathrm{r}^2 + R_i^2)N_i^2} = 1 - h_i(c_\mathrm{l}, c_\mathrm{r}) \tag{11b}$$

Where $h_i(c_\mathrm{l}, c_\mathrm{r})$ is a non linear function of the unknown scalar variables – $c_\mathrm{l}, c_\mathrm{r}$, while for each $[x_i, y_i]$ coordinates, $N_i$ and $R_i$ are known. Now, if we substitute Eq. (11) into $f_{\mathrm{Lin}}(R_{\mathrm{ml};i}, R_{\mathrm{rad};i})$ in Eq. (7), we derive the following relation between $f_{\mathrm{Lin}}(R_{\mathrm{ml};i}, R_{\mathrm{rad};i})$ and $h_i(c_\mathrm{l}, c_\mathrm{r}) \triangleq h_i$, that is:

$$f_{\mathrm{Lin}}(R_{\mathrm{ml};i}, R_{\mathrm{rad};i}) = h_i R_{\mathrm{rad};i} + (1 - h_i(c_\mathrm{l}, c_\mathrm{r}))R_{\mathrm{ml};i} \tag{12}$$





AMTD
7, 4481–4528, 2014

where in Eq. (12) one can see that $0 \leq h_i \leq 1$.

Now, by defining $R_{g;i}$ as the "true" rain intensity at each $[x_i, y_i]$ coordinate, as measured by the rain gauges, we offer to minimize the cost function, as defined in Eq. (13), in order to derive the optimal solution for the unknown variables (i.e., for $[c_l, c_r]$):

$$C(c_l, c_r) = \sum_i (h_i R_{\mathrm{rad};i} + (1 - h_i) R_{\mathrm{ml};i} - R_{g;i})^2 \quad (13)$$

By minimizing $C(c_l, c_r)$ in Eq. (13), we may derive our estimate for $[c_l, c_r]$, which is given by:

$$[\hat{c}_l, \hat{c}_r] = \underset{c_l, c_r}{\mathrm{argmin}}\{C(c_l, c_r)\} \quad (14)$$

We point out that each $R_{g;i}$ (denoted as the rain gauge in the $[x_i, y_i]$ coordinate) provides measurements of the amount of rain (in mm), for a certain amount of time. Thus, in order to derive the desired estimates, as shown in Eq. (14), we analyzed three heavy rain events, which occurred over the last 5 years in Israel, specifically on: 18 January 2010, 7–10 January 2013 and 30 December 2009. We derived an estimate for the unknown variables $[c_l, c_r]$ using the rain intensities available from the radar, ML, and rain gauges for all available coordinates, where each inspected coordinate satisfied Condition 3 from above, and a rain gauge measurement was available at that coordinate as well. The non linear estimation problem in Eq. (14) might be solved in various ways (e.g., Marquardt, 1963; Wan and Van Der Merwe, 2000). In this research we used a nonlinear least squares iterative method, as detailed in Byrd et al. (1987).

## 3 Results

This section describes the results of the rainfall measurements from different sources (only radar, only ML, and the offered integrated method). The first two parts define the study area and parameter estimation, respectively. In the second part we present the





AMTD
7, 4481–4528, 2014

results including reconstructed maps, scatter plots, tables and graphs showing statistical and numerical comparisons.

### 3.1 Study area

The study area is located in the center of Israel (approximately 22 000 km$^2$), where both radar and ML data are available. Most of the region (from the north to the center) is covered by the IMS radar, located in Bet-Dagan, as shown in Fig. 1, where the areas covered by ML are also delineated.

The rain rates for calibration and validation of the rainfall measurements were recorded by 70 rain gauges distributed in space (see Fig. 3). Moreover, the total attenuation of 96 operational telecommunication ML were also used. The ML operate at a time resolution of 15 min. The radar operates in a spatial resolution of 1 km$^2$ with 5 min time intervals. The rain gauge network, composed of 70 tipping-bucket gauges, provide measurements at a time resolution of 10 min.

In order to make the data from the rain gauges, ML, and radar comparable, we inspect only the common times which occur every 30 min (i.e., at: 00:00, 00:30. . . 23:30 IDT (Israe Daylight Time)). The ML used in this application operate at 18–23 GHz, with horizontal (or vertical) polarization, with lengths that vary between 3–20 Km and with a magnitude resolution of 0.1 db. The reconstruction adopted for the ML is the instantaneous rain field reconstruction developed by Liberman et al. using sparse rain field modelling, as described in Sect. 1.2, though, as mentioned before, any reconstruction technique can be applied (e.g., Zinevich and Alpert, 2010; Overeem et al., 2013) for the proposed analysis.

### 3.2 Parameter estimation

For the estimation of the parameters, we used 40 different points in space, all of which had available data from all sources. Given that, we have chosen 2 of the 3 events mentioned above for the provided analysis of the new technique by using a leave-one-out





AMTD
7, 4481–4528, 2014

procedure for calibration and validation of the measurements. Specifically, for the set of rain events (1), (2) and (3), only data from the other two events are used as follows:

1. Event (1): 7–10 January 2013, 30 December 2009.
2. Event (2): 18 January 2010, 30 December 2009.
3. Event (3): 7–10 January 2013, 18 January 2010.

Given the large amount of data, we assume that the estimations will be similar for all inspected events. The nonlinear least squares iterative unique solution yielded the following estimation results for each of the examined events:

$$[\hat{c}_{\mathrm{l}}, \hat{c}_{\mathrm{r}}]_{\mathrm{Event}_{(1)}} = [9.82, 98.89] \tag{15a}$$

$$[\hat{c}_{\mathrm{l}}, \hat{c}_{\mathrm{r}}]_{\mathrm{Event}_{(2)}} = [10.64, 100.17] \tag{15b}$$

$$[\hat{c}_{\mathrm{l}}, \hat{c}_{\mathrm{r}}]_{\mathrm{Event}_{(3)}} = [10.45, 101.02] \tag{15c}$$

where $[\hat{c}_{\mathrm{l}}, \hat{c}_{\mathrm{r}}]$ are denoted as the estimations for $[c_{\mathrm{l}}, c_{\mathrm{r}}]$, for their respective events. While the $\hat{c}_{\mathrm{r}}$ values are similar, there is about 8 % difference in the $\hat{c}_{\mathrm{l}}$ estimations of event (1) with respect to events (2) and (3). However, they are still close enough to provide reliable estimations. Moreover, as the number of measurements from rain events increases, the parameter estimation will be stronger, hence improving the application of the algorithm in the future. In short, using these values, we assume an optimal linear weighted integration when using radar and ML for the purpose of rain field reconstruction for each of the inspected set of events (1), (2) and (3).

### 3.3 The reconstruction evaluation

In order to best evaluate the performance of the different measuring techniques, we present both the rainfall maps and comparative statistics. For the purpose of comparing





AMTD
7, 4481–4528, 2014

Integration between WSN and radar for improved rainfall mapping

Y. Liberman et al.

the different measurements to real rain intensity over several coordinates in space, we calculate the spatial correlation, RMSE and RB, which are defined as follows:

$$\rho = \frac{\frac{1}{NM}\sum_{j=1}^{M}\sum_{i=1}^{N}(\hat{x}_{i,j}-\mu_{\hat{x}})(x_{i,j}-\mu_x)}{\frac{1}{NM}\sqrt{\sum_{j=1}^{M}\sum_{i=1}^{N}(x_{i,j}-\mu_x)^2\sum_{j=1}^{M}\sum_{i=1}^{N}(\hat{x}_{i,j}-\mu_{\hat{x}})^2}} \tag{16a}$$

$$\mathrm{RMSE} = \sqrt{\frac{1}{NM}\sum_{j=1}^{M}\sum_{i=1}^{N}(\hat{x}_{i,j}-x_{i,j})^2} \tag{16b}$$

$$\mathrm{RB} = \frac{1}{NM}\sum_{j=1}^{M}\sum_{i=1}^{N}\frac{\hat{x}_{i,j}-x_{i,j}}{x_{i,j}} \times 100 \tag{16c}$$

Where $\rho$ is defined as the spatial correlation, the RMSE is defined as the Spatial Root Mean Square Error, and RB is the Relative Bias (in %). In Eq. (16), $\mu_{\hat{x}} = \frac{1}{NM}\sum_{j=1}^{M}\sum_{i=1}^{N}\hat{x}_{i,j}$ ; $\mu_x = \frac{1}{NM}\sum_{j=1}^{M}\sum_{i=1}^{N}x_{i,j}$ are defined as the mean spatial rain rates of the estimated rain measurements and the true measurements, respectively. In Eq. (16), the index $j$ refers to each time step (total of $M$ time steps), while index $i$ refers to the spatial coordinate (total of $N$ coordinates), which corresponds to each $[x_i, y_i]$ coordinate.

In Figs. 4, 5 and 6, the rain field reconstructions estimated by the different sources: rain gauges, radar, ML, and the integrated method are illustrated. Maps are shown for a given time step for each of the analyzed events (i.e., 18 January 2010 at 17:00, 9 January 2013 at 14:30 and 30 December 2009 at 16:00 IDT). From the figures, it is clear that the integrated method expands the spatial coverage substantially. In addition, it improved the estimations for many of the areas where radar coverage is poor and ML exist, specifically the area of Mitzpe Ramon. As it can be observed, the radar cannot provide an estimate for the rain rate if the distance between the radar to a coordinate in space is higher than 150 km, as was also discussed in Sect. 1.1.

Figures 7, 8 and 9 show the performance evaluation for the set of events (1), (2) and (3), respectively. The correlation coefficient (spatial correlation) and the RMSE are





AMTD
7, 4481–4528, 2014

shown, both evaluated for the common times spanning the rain event. Each line in the figures is the comparison between one of the sources as compared to the real rain intensity measured by the rain gauges. The added value of the integrated technique is evident in its lower RMSE and RB, while showing higher correlation values in all events. The performance evaluation of all methods over the entire event (for all the events) is shown in Table 1 (mean spatial correlation), Table 2 (RMSE) and Table 3 (RB).

Furthermore, we had also evaluated the Probability of Detection (POD), the False Alarm Ratio (FAR) and the Critical Success Index (CSI) on the proposed integration technique. These measures are very important criterions for assessing the quality of the method. For this, we use the definition of the relative error, i.e.: $\phi \triangleq \frac{|\hat{x}-x|}{x}$), where $x$ denotes a rain gauges (ground truth) measurement and $\hat{x}$ is the rain intensity estimation at the same point. Thus, a Success is declared if $\phi < \epsilon$ (e.g., $\epsilon = 10\,\%$), otherwise it is regarded as a Miss. A false alarm is declared if a rain gauge indicated no rain but the estimation did. Given that definitions, by denoting: $S$ – Total successes, $M$ – Total misses, and $F$ – Total false alarms, the given criterions can be evaluated by: $\text{POD} \triangleq \frac{S}{M+S}$; $\text{FAR} \triangleq \frac{F}{F+S}$; $\text{CSI} \triangleq \frac{S}{S+M+F}$. By considering all the available rain gauges measurements, for all the inspected events at all given time frames, the integration algorithm achieved the impressive scores of (with $\epsilon = 10\,\%$): POD $\approx 89\,\%$, FAR $\approx 12\,\%$, and CSI $\approx 81\,\%$. This results once again proves the high quality of the proposed integration technique. It should be noted that even when we used lower value of $\epsilon$, similar results were achieved.

Figures 10, 11 and 12 demonstrate the scatter plots, each with its corresponding regression line (black line) for the set of events (1), (2) and (3), respectively. From these figures it is clear that the disparity of the points is the lowest for the integration algorithm with respect to the ML and the Radar scatter plots (due to the under and over estimation of their reconstructions). This implies that the integrative approach is the most accurate one.

The highest correlations, lowest RMSE and lowest (absolute) RB for all three rain events were obtained using the integration algorithm. From both the maps and the





AMTD
7, 4481–4528, 2014

comparative statistics, the integrated method provides a new way to improve rainfall estimation spatially and over time. The rightness of using this particular integration scheme, as in Eq. (7), can be understood by examining the RB of the Radar and ML, which showed an over and under estimation, respectively, for all the inspected events.

Our last analysis of the data was comparing the total accumulated rainfall over a specific point in the study area for the duration of the rain event. The accumulated rain was calculated as follows:

$$R(T_k) = \int_0^{T_k} r_{ij}\mathrm{d}t \approx \sum_{r=0}^{T_k} r_{ij}(T_\mathrm{r})\Delta T \text{ (mm)} \tag{17}$$

where $r_{ij}$ is the rain rate ($\mathrm{mm\,h^{-1}}$) in the $[x_i, y_j]$ coordinate, $\Delta T$ is the time resolution (e.g., for the rain gauges 1/6 h). $T_k$ is the accumulation time, and $T_\mathrm{r}$ indicates each time sample for each $r_{ij}$ (i.e., $r_{ij}(T_\mathrm{r})$ is the rain rate at time $T_\mathrm{r}$, expressed in $\mathrm{mm\,h^{-1}}$). $R(T_k)$ indicates the accumulated rain for each $T_k$ (e.g., for $T_k$ = 00:30, $R(T_k)$ is the accumulated rain from 00:00 to 00:30).

The sites, Dorot and Ramle, were chosen for their respective rain events given the availability of their nearby ML data, as well as their distance from the radar. The data availability from the sources, for each site, is detailed as follows:

1. *Ramle site*: [31.83° N, 34.96° E], 18 January 2010: 24 h of rain event, 30 operating ML in the area of interest (as shown in Fig. 13), provided by Pelephone, are available. The links operate at a frequency of 18–23 Ghz (for each link) and the link lengths vary between 1–15 km. The RSL data from the ML is given at a time resolution of 1 min with magnitude resolution of 1 db. Distance from Bet Dagan radar is 17.12 km.

2. *Dorot site*: [31.50° N, 34.64° E], 7–10 January 2010: 96 h of rain event, and 30 December 2009: 24 h of rain event. 12 operating ML in the area of interest (as shown in Fig. 13), provided by Cellcom ltd, are available. The ML operate at a frequency





AMTD
7, 4481–4528, 2014

of 17–21 Ghz (for each link) and each link length varies between 1–13. Distance from Bet Dagan radar is 53.67 km. The RSL data from the links is given at a temporal resolution of 15 min with a magnitude resolution of 0.1 db.

It should be noted that for each site we calculated the accumulated rainfall over the duration for the set of events (1), (2) and (3). Given that the time step varies between methods, we interpolated the accumulated results to a 5 min time resolution using Cubic Spline interpolation (De Boor, 1978) in order to make the accumulation results comparable. That is, when regarding the rain gauges for example, the time interval is 10 min, i.e.: 00:00, 00:10. . . 23:50 IDT, thus, after interpolation the results correspond to time samples every 5 min, i.e. at: 00:05, 00:10, 00:15. . . 23:55 IDT.

An illustration of the scatter plots, each with its corresponding regression line (black line), for Ramle (event (1)) and Dorot (events (2) and (3)) sites is provided in Figs. 14, 15 and 16. From these figures it is clear that the integration approach achieved the lowest disparity of the points (with respect to the regression line) when comparing to the ML and the Radar scatter plots. This not only implies that the integrative approach is the most accurate one, but also proves the rightness in using Eq. (7) for the proposed integration scheme, both spatially and temporally.

Finally, Figs. 17 and 18 illustrate the accumulated rain intensity for Ramle (event (1)) and Dorot (events (2) and (3)) sites. The results are demonstrated for each source, i.e.: the radar (pink straight line), rain gauges (black straight line), the integration (dashed red line) and the ML (dash-dot blue line) every 5 min (i.e., the accumulated rain during the rain event – as defined in Eq. 17).

From Figs. 17 and 18 one can see that the integration procedure improved the estimation of the accumulated rain, specifically for the radar which had an overestimation in all cases. When compared with ML measurements, for events (2) and (3) at Dorot, the ML showed an underestimation of the accumulation, due to the rather sparse network deployed (only 12 available ML) in the area. On the other hand, the integrated method provides a clear, impressive improvement. As expected, for Ramle site, there is no evident improvement of the integrated method, not in total amounts, nor with regard





AMTD
7, 4481–4528, 2014

to correlation (on the instantaneous rain rate) or the RMSE (on the accumulated rain) when compared to the ML. Whereas when comparing the performance to that of the radar an evident improvement was. This is due to the high number of ML available at that point. To calculate the RMSE, RB and spatial correlation metrics we use Eq. (16) with $N = 1$, that is, the performance measures are calculated with respect to one coordinate in space with $M$ different time steps. The evaluation is derived at the common times for all the reconstruction methods (i.e., every 30 min – 00:00, 00:30...23:30 IDT) during the whole rain event. These calculations are shown for Ramle site in Table 4, and for Dorot site in Tables 5 and 6, with respect to events (2) and (3). These results (and especially the RB results) of all methods prove once again the unwavering ability of the novel integration technique.

## 4 Conclusions

The ability to accurately monitor rainfall at high spatial and temporal scales is critical for meteorological and hydrological research and applications. Each of the techniques currently available (rain gauges, radar, ML and satellites) can provide important information. Each, however, have their limitations, yet they can be used to greatly complement one another. Here we present a novel method for data fusion of different rainfall mapping sources, while optimizing the advantages of each. The integration technique achieves an optimal weighted linear estimation of the rain field, while mainly considering the pros and cons of each source, mainly the coverage area of the ML and the weather radar. We have shown that compared to both spatially averaged rain gauges (Figs. 7, 8 and 9) as well as in specific locations (i.e., Figs. 17 and 18), the integrated approach is capable of reconstructing reliable and accurate 2-D rainfall maps.

By using data from rain gauges from several coordinates in space, and over multiple rain events, we achieved an estimation for the unknown parameters in the integration model. This parameter estimation can be improved in the future as data from additional rain events become available. The main limitations of this approach lie in the necessity





AMTD
7, 4481–4528, 2014

to have a specific model for the integration. In this paper we chose the use of a weighted linear model, the rightness of using this kind of model can be understood from both the RB metric (Table 3) and the scatter plots (Figs. 10–12).

The methodology proposed here is computationally fast and provides improved estimated rainfall over the entire Israel region. The data used in the analysis here shows how maps can be drawn from the different sources in a manner allowing them to be compared, contrasted and complimentary one toward the other, in an effort to provide the most robust assessment possible. The limitations obviously are the availability of data. Specifically, the ML data are subject to specific time resolution with arbitrary distribution in space, as provided by the telecommunication companies. However, once the data is accessible, we may manipulate the data into uniform formats, and calibrate the necessary parameters in order to provide 4 complementary 2-D rainfall maps which can be used both to better inform meteorological and hydrological models as well as potentially give a better understanding of the underlying dynamics of the storm, which no one as never provided before.

Even though the proposed integration technique was proven to yield very accurate results, future work could focus on more complex (e.g., non-linear) models for integration between the sources, and the use of additional sources (e.g., satellite) for improved accuracy of the rain field reconstruction.

*Acknowledgements.* The authors would deeply like to thank Y. Dagan (Cellcom ltd.), N. Dvela and A. Shilo (Pelephone) for the long term cooperation and for providing the data for this research. We also thank the IMS Service for meteorological data. Partial Funding for RS and PA was provided by the BSF, DESERVE projects.

## References

Alpert, P., Shafir, H., Cotton, W. R., and Freundlich, A.: Prediction of Meso-gamma scale orographic precipitation, Trends In Hydrology, 1, 401–441, 1994. 4483

Bringi, V. and Chandrasekar, V.: Polarimetric Doppler Weather Radar: Principles And Applications, Cambridge University Press, 2001. 4485

Byrd, R. H., Schnabel, R. B., and Shultz, G. A.: A trust region algorithm for nonlinearly constrained optimization, SIAM J. Numer. Anal., 24, 1152–1170, 1987. 4493

Chahine, M. T., Pagano, T. S., Aumann, H. H., Atlas, R., Barnet, C., Blaisdell, J., Chen, L., Divakarla, M., Fetzer, E. J., Goldberg, M., Gautier, C., Granger, S., Hannon, S., Irion, F. W., Kakar, R., Kalnay, E., Lam-brigtsen, B. H., Lee, S. Y., Le Marshall, J., and McMillan, W. W.: AIRS improving weather forecasting and providing new data on greenhouse gases, Bull. Am. Meteorol. Soc., 7, 911–926, 2006. 4489

Chen, S. S., Donoho, D. L., and Saunders, M. A.: Atomic decomposition by basis pursuit, SIAM J. Sci. Comput., 20, 33–61, 1998. 4487

Chwala, C., Gmeiner, A., Qiu, W., Hipp, S., Nienaber, D., Siart, U., Eibert, T., Pohl, M., Seltmann, J., Fritz, J., and Kunstmann, H.: Precipitation observation using microwave backhaul links in the alpine and pre-alpine region of Southern Germany, Hydrol. Earth Syst. Sci., 16, 2647–2661, doi:10.5194/hess-16-2647-2012, 2012. 4486

Daley, R.: Atmospheric Data Analysis, vol. 2, Cambridge University Press, 1993. 4490

De Boor, C.: A Practical Guide to Splines, vol. 27, Springer-Verlag, New York, 1978. 4499

Doviak, R. J., Zrnic, D. S., and Sirmans, D. S.: Doppler weather radar, Proc. IEEE, 67, 1522–1553, 1979. 4485

Eldar, Y. C.: Sampling with arbitrary sampling and reconstruction spaces and oblique dual frame vectors, J. Fourier Anal. Appl., 9, 77–96, 2003. 4490

Germann, U., Galli, G., Boscacci, M., and Bolliger, M.: Radar precipitation measurement in a mountainous region, Q. J. Roy. Meteor. Soc., 132, 1669–1692, 2006. 4484

Goldshtein, O., Messer, H., and Zinevich, A.: Rain rate estimation using measurements from commercial telecommunications links, IEEE T. Signal Proces., 57, 1616–1625, 2009. 4486

Liberman, Y.: Optimal Recovery of Rainfall Maps Using Measurements from Wireless Sensors Network, M.Sc. Thesis, Tel Aviv University, 2013. 4486, 4490

Mackenzie, A. I., Baxa Jr, E., and Harrah, S. D.: Characterization of urban ground clutter with new generation airborne Doppler weather radar, in: Radar Conference, 1993, Record of the 1993 IEEE National, 51–56, IEEE, 1993. 4483, 4485

Marquardt, D. W.: An algorithm for least-squares estimation of nonlinear parameters, J. Soc. Ind. Appl. Math., 11, 431–441, 1963. 4493

Marshall, J. S., Langille, R. C., and Palmer, W. McK: Measurements of rainfall by radar, J. Meteorol., 4, 186–192, 1947. 4484





AMTD
7, 4481–4528, 2014

Integration between WSN and radar for improved rainfall mapping

Y. Liberman et al.

McLaughlin, D.: An integrated approach to hydrologic data assimilation: interpolation, smoothing, and filtering, Adv. Water Resour., 25, 1275–1286, 2002. 4489

Meischner, P., Bringi, V., Heimann, D., and Höller, H.: A squall line in southern Germany: kinematics and precipitation formation as deduced by advanced polarimetric and Doppler radar measurements, Mon. Weather Rev., 119, 678–701, 1991. 4485

Messer, H., Zinevich, A., and Alpert, P.: Environmental monitoring by wireless communication networks, Science, 312, p. 713, 2006. 4483, 4486

Morin, E., Krajewski, W., Goodrich, D., Gao, X., and Sorooshian, S.: Estimating rainfall intensities from weather radar data: the scale dependency problem, J. Hydrometeorol., 4, 782–797, 2003. 4484

Morin, E., Goodrich, D. C., Maddox, R. A., Gao, X., Gupta, H. V., and Sorooshian, S.: Spatial patterns in thunderstorm rainfall events and their coupling with watershed hydrological response, Adv. Water Resour., 29, 843–860, 2006. 4487

Olsen, R.: The $\alpha R^{\beta}$ relation in the calculation of rain attenuation, IEEE T. Antenn. Propag., 26, 318–329, 1978. 4485

Örs, T., Chotikapong, Y., and Sun, Z.: Bisante Deliverable 2.2: GEO Satellite Network Characteristics, 1999. 4486, 4487

Overeem, A., Leijnse, H., and Uijlenhoet, R.: Measuring urban rainfall using microwave links from commercial cellular communication networks, Water Resour. Res., 47, W12505, doi:10.1029/WR-47-1035-2011, 2011. 4486

Overeem, A., Leijnse, and Uijlenhoet, L. R.: Country wide rainfall maps from CMN, P. Natl. Acad. Sci. USA, 110, 2741–2745, 2013. 4486, 4494

Prat, O. P. and Barros, A. P.: Exploring the transient behavior of Z-R relationships: implications for radar rainfall estimation, J. Appl. Meteorol. Clim., 48, 2127–2143, 2009. 4485

Sendik, O. and Messer, H.: On the reconstructability of images sampled by random line projections, in: Electrical & Electronics Engineers in Israel (IEEEI), 2012 IEEE 27th Convention of, 1–5, IEEE, 2012. 4489

Skolnik, M. I.: Introduction to Radar, Radar Handbook, McGraw-Hill Incorporated, 1990–1993, 1962. 4485, 4488

Sorooshian, S., AghaKouchak, A., Arkin, P., Eylander, J., Foufoula-Georgiou, E., Harmon, R., Hendrickx, J. M., Imam, B., Kuligowski, R., Skahill, B., and Gail. S. J.: Advancing the remote sensing of precipitation, B. Am. Meteorol. Soc., 92, 1271–1272, 2011. 4483

Wan, E. A. and Van Der Merwe, R.: The unscented Kalman filter for nonlinear estimation, in: Adaptive Systems for Signal Processing, Communications, and Control Symposium 2000, 153–158, IEEE, 2000. 4493

Zinevich, A., Messer, H., and Alpert, P.: Prediction of rainfall intensity measurement errors using commercial microwave communication links, Atmos. Meas. Tech., 3, 1385–1402, doi:10.5194/amt-3-1385-2010, 2010. 4494





AMTD

7, 4481–4528, 2014

Integration between WSN and radar for improved rainfall mapping

Y. Liberman et al.

**Table 1.** Spatial correlation of all methods for all time steps.

| | event (1) | event (2) | event (3) |
|---|---|---|---|
| ML | 0.74 | 0.79 | 0.76 |
| Radar | 0.64 | 0.69 | 0.71 |
| Integration | 0.87 | 0.86 | 0.88 |





AMTD
7, 4481–4528, 2014

**Table 2.** RMSE (mm $h^{-1}$) of all methods for all time steps.

| | Event (1) | Event (2) | Event (3) |
|---|---|---|---|
| ML | 3.70 | 3.11 | 3.86 |
| Radar | 6.03 | 4.91 | 4.89 |
| Integration | 2.26 | 2.01 | 1.98 |





AMTD
7, 4481–4528, 2014

**Table 3.** Relative Bias (%) of all methods for all time steps.

| | event (1) | event (2) | event (3) |
|---|---|---|---|
| ML | −12 | −15 | −18 |
| Radar | 17 | 13 | 20 |
| Integration | 7 | −3 | 4 |





AMTD
7, 4481–4528, 2014

**Table 4.** Performance analysis Event (1) – Ramle site.

| | Correlation | RMSE (mm) | Relative Bias (%) |
|---|---|---|---|
| ML | 0.87 | 3.93 | −3 |
| Radar | 0.71 | 14.31 | 20 |
| Integration | 0.87 | 3.89 | −3 |





AMTD
7, 4481–4528, 2014

**Table 5.** Performance analysis Event (2) – Dorot site.

| | Correlation | RMSE (mm) | Relative Bias (%) |
|---|---|---|---|
| ML | 0.77 | 6.09 | −21 |
| Radar | 0.68 | 9.19 | 19 |
| Integration | 0.88 | 2.07 | −6 |





AMTD
7, 4481–4528, 2014

**Table 6.** Performance analysis Event (3) – Dorot site.

| | Correlation | RMSE (mm) | Relative Bias (%) |
|---|---|---|---|
| ML | 0.75 | 6.68 | −29 |
| Radar | 0.72 | 7.79 | 34 |
| Integration | 0.86 | 2.07 | 7 |





AMTD

7, 4481–4528, 2014

Integration between WSN and radar for improved rainfall mapping

Y. Liberman et al.

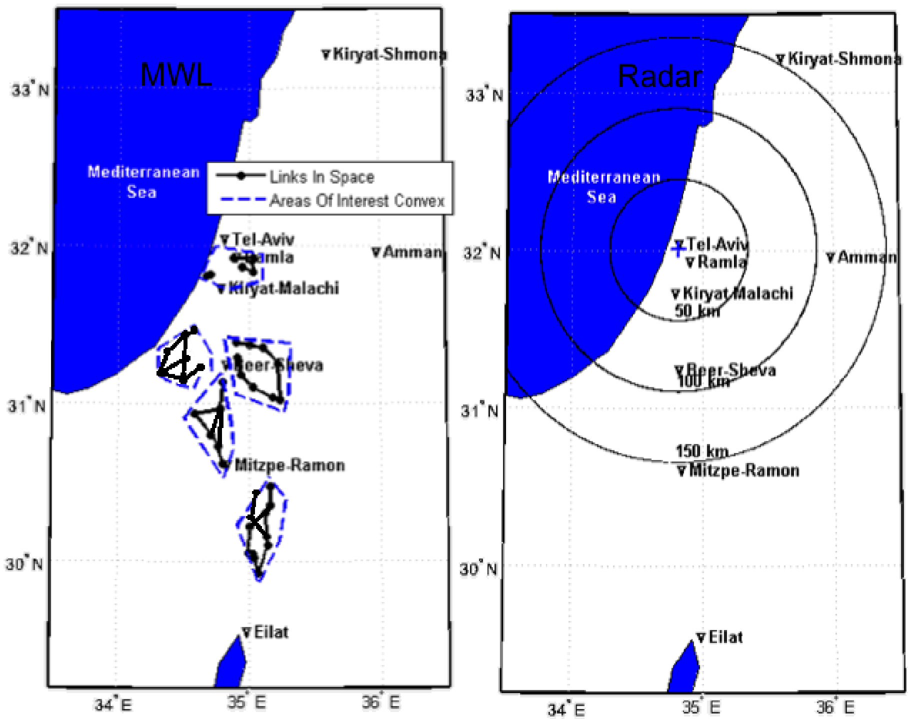


**Fig. 1.** Left: 96 ML in space divided into 6 areas of interest. Black lines indicate the links, and the blue dashed lines indicate the convex of each area of interest. Right: the radar coverage area, where the blue "+" sign indicates the radar coordinates – Bet Dagan. The radar's 50, 100, and 150 km radius distances are also indicated.





AMTD
7, 4481–4528, 2014

Integration between WSN and radar for improved rainfall mapping

Y. Liberman et al.

Title Page
Abstract | Introduction
Conclusions | References
Tables | Figures
◀| |▶
◀ ▶
Back | Close
Full Screen / Esc
Printer-friendly Version
Interactive Discussion

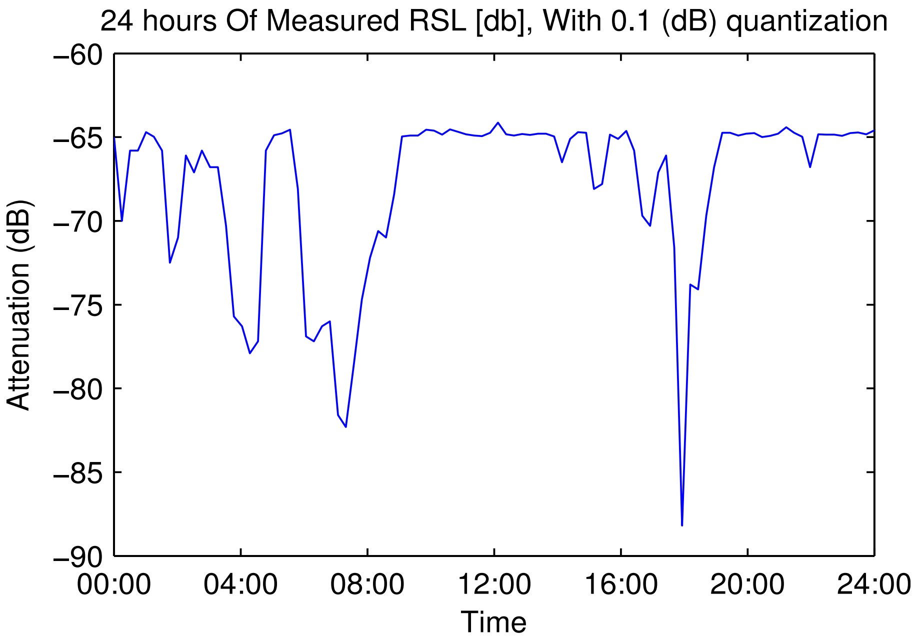


**Fig. 2.** Example of 24 h of measured RSL (dB), during a rain event which occurred on 7 January 2013, for a single 14 km link, operating at a frequency of 21.8 GHz.





AMTD
7, 4481–4528, 2014

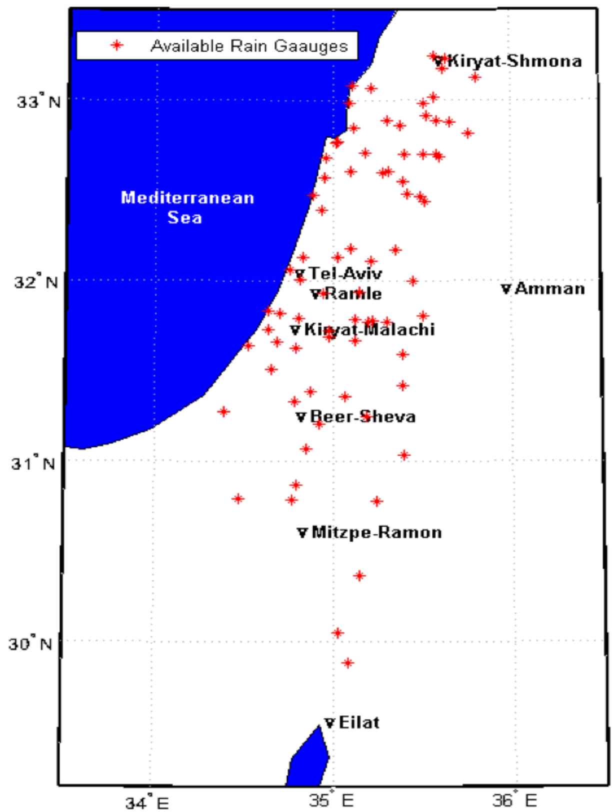


**Fig. 3.** 70 available rain gauges in space, each red "+" sign indicates a rain gauge location in space.





AMTD
7, 4481–4528, 2014

Integration between WSN and radar for improved rainfall mapping

Y. Liberman et al.

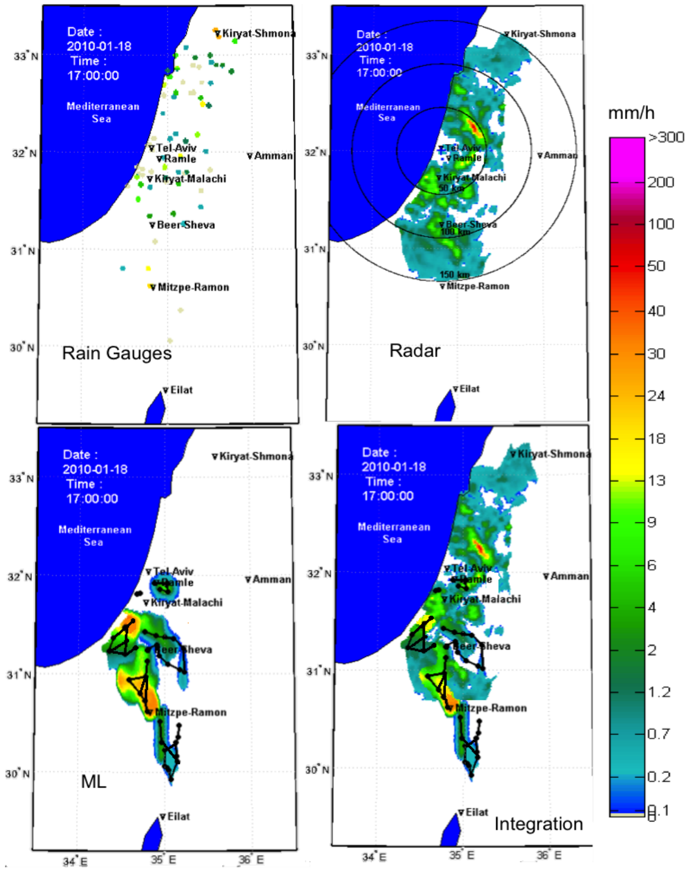


**Fig. 4.** Example of the rain field reconstruction for the 18 January 2010 rain event (event(1)) at 17:00. Top left: rain gauges. Top right: radar. Bottom left: ML. Bottom right: the proposed integration.





AMTD
7, 4481–4528, 2014

Integration between WSN and radar for improved rainfall mapping

Y. Liberman et al.

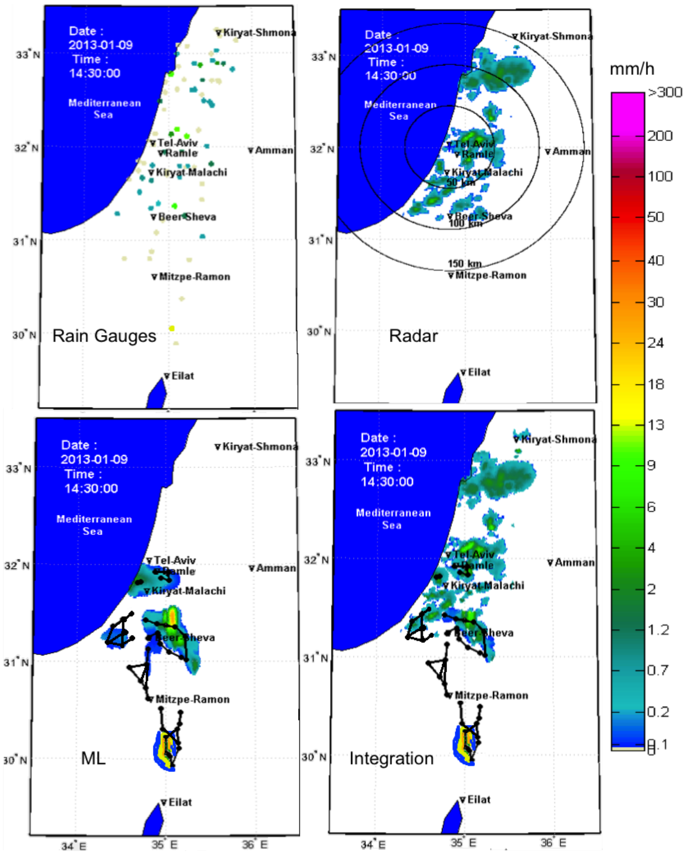


**Fig. 5.** Example of the rain field reconstruction for the 9 January 2013 rain event (event (2)) at 14:30. Top left: rain gauges. Top right: radar. Bottom left: ML. Bottom right: the proposed integration.

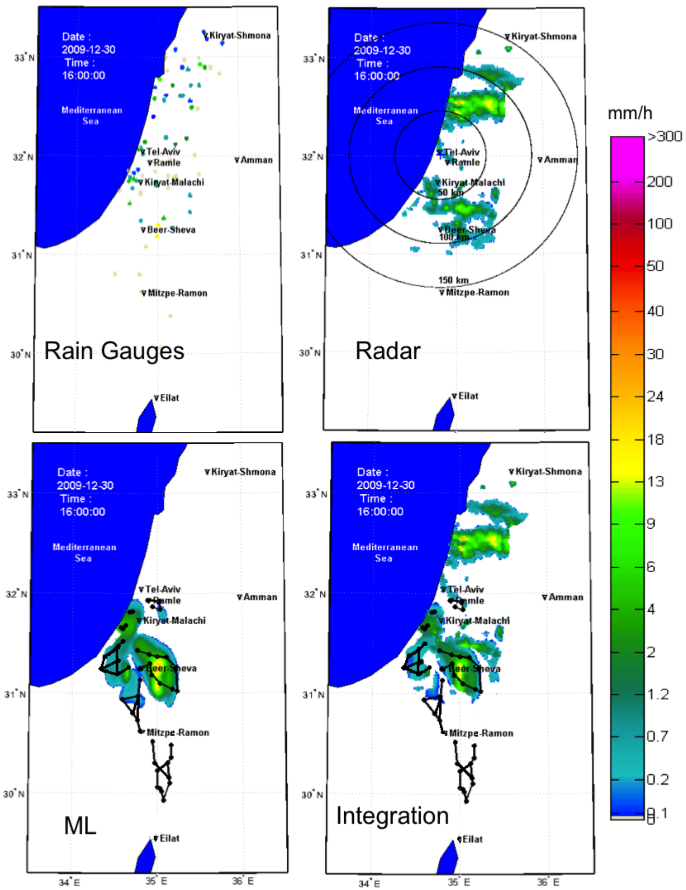


**Fig. 6.** Example of the rain field reconstruction for the 30 December 2009 rain event (event (3)) at 16:00. Top left: rain gauges. Top right: radar. Bottom left: ML. Bottom right: the proposed integration.





AMTD
7, 4481–4528, 2014

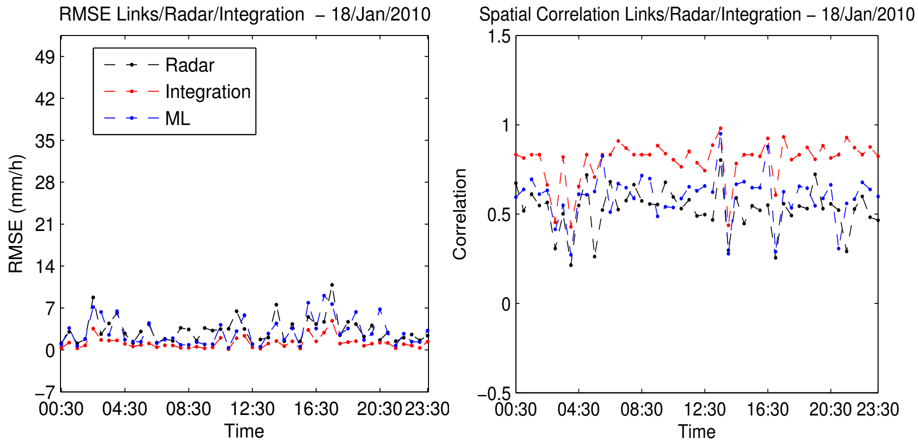


**Fig. 7.** Evaluation analysis of event (1), where the radar (black line), the proposed integration technique (red line) and the ML (blue line) are compared to the rain gauges at the common times. Left: RMSE. Right: spatial correlation.

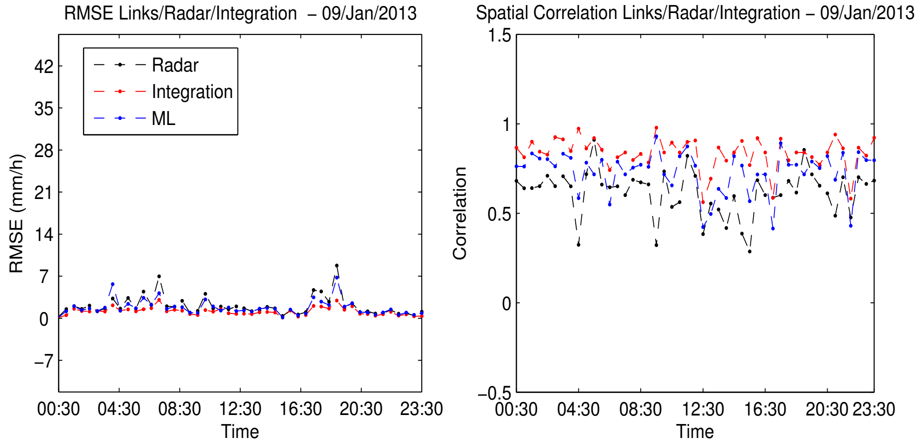


**Fig. 8.** Evaluation analysis of event (2), where the radar (black line), the proposed integration technique (red line) and the ML (blue line) are compared to the rain gauges at the common times. Left: RMSE. Right: spatial correlation.





AMTD
7, 4481–4528, 2014

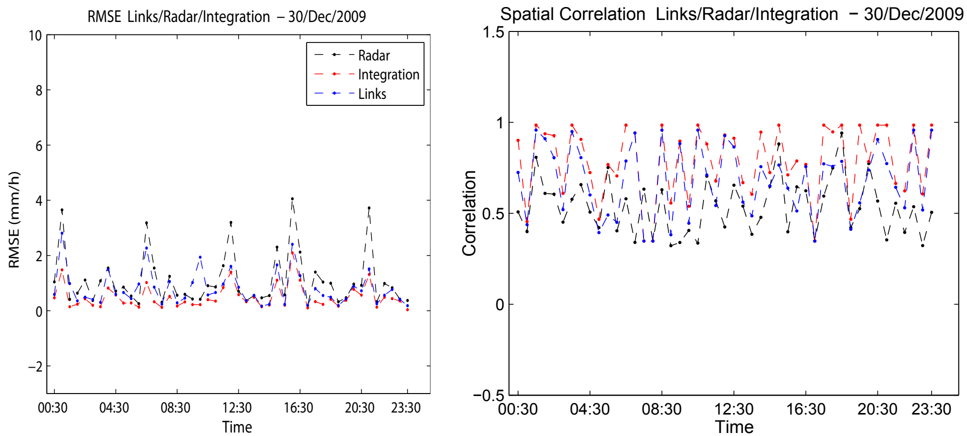


**Fig. 9.** Evaluation analysis of event (3), where the radar (black line), the proposed integration technique (red line) and the ML (blue line) are compared to the rain gauges at the common times. Left: RMSE. Right: spatial correlation.

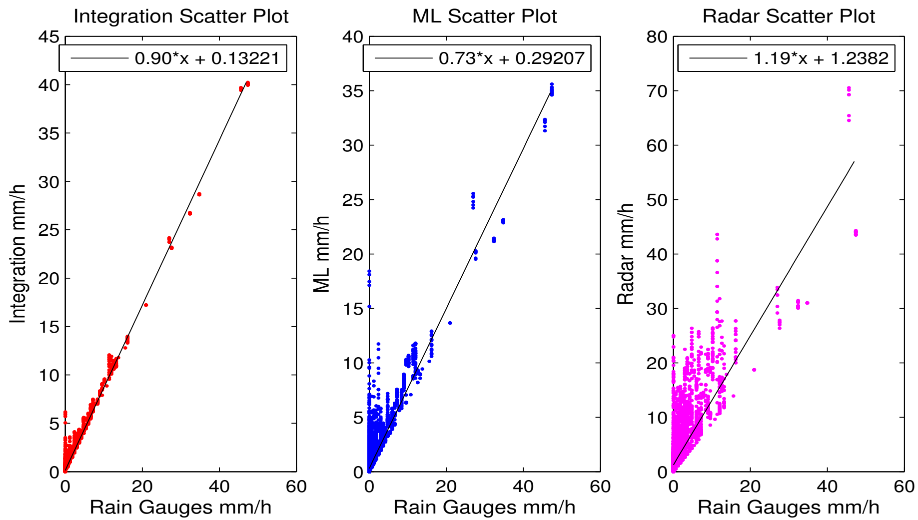


**Fig. 10.** Rain rates scatter plots of the integration (left), the ML (middle) and the radar (right) with respect to all the available rain gauges for event (1).





AMTD
7, 4481–4528, 2014

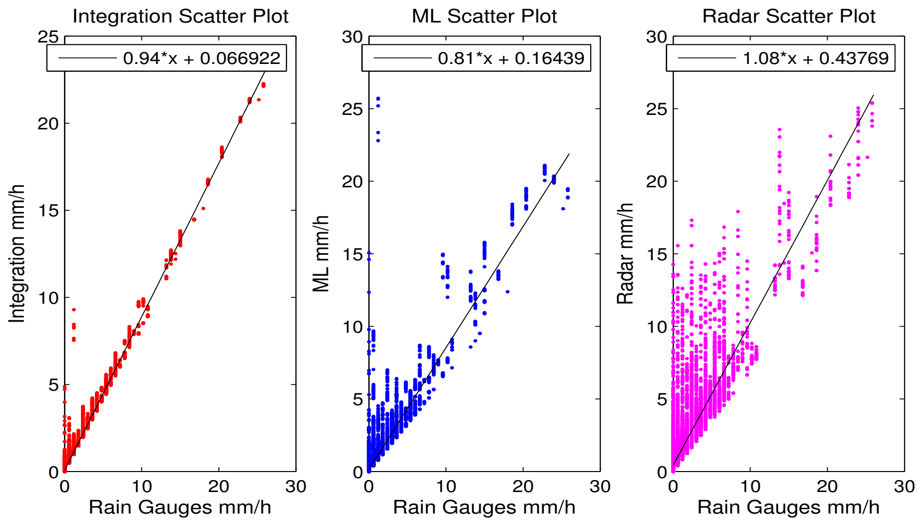


**Fig. 11.** Rain rates scatter plots of the integration (left), the ML (middle) and the radar (right) with respect to all the available rain gauges for event (2).





AMTD
7, 4481–4528, 2014

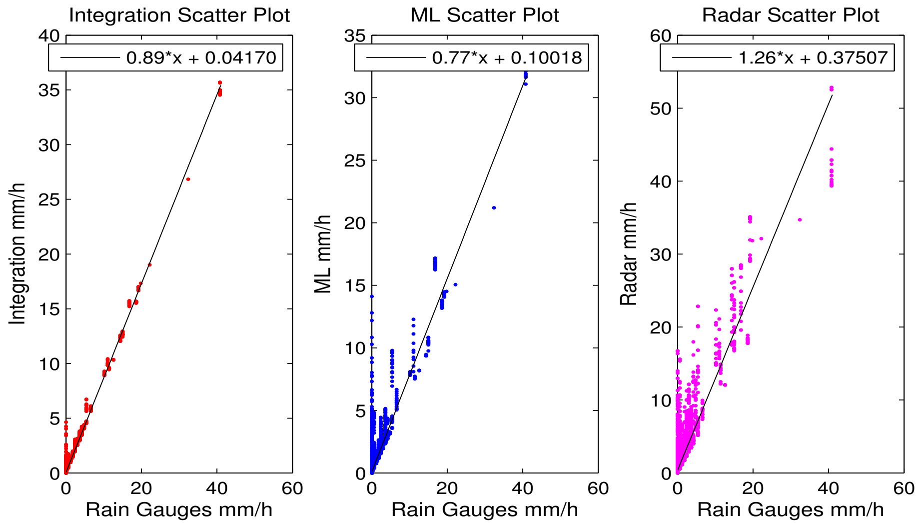


**Fig. 12.** Rain rates scatter plots of the integration (left), the ML (middle) and the radar (right) with respect to all the available rain gauges for event (3).





AMTD
7, 4481–4528, 2014

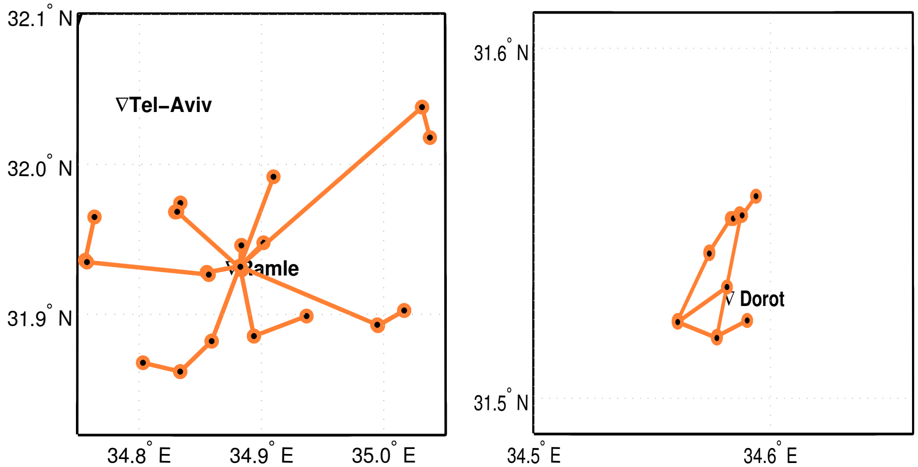


**Fig. 13.** ML distribution for two different coordinates. Left: Ramle coordinate, in an area of about 400 $km^2$, for 30 ML provided by Pelephone Ltd. Right: Dorot coordinate in an area of about 150 $km^2$, for 12 ML provided by Cellcom ltd.



AMTD
7, 4481–4528, 2014

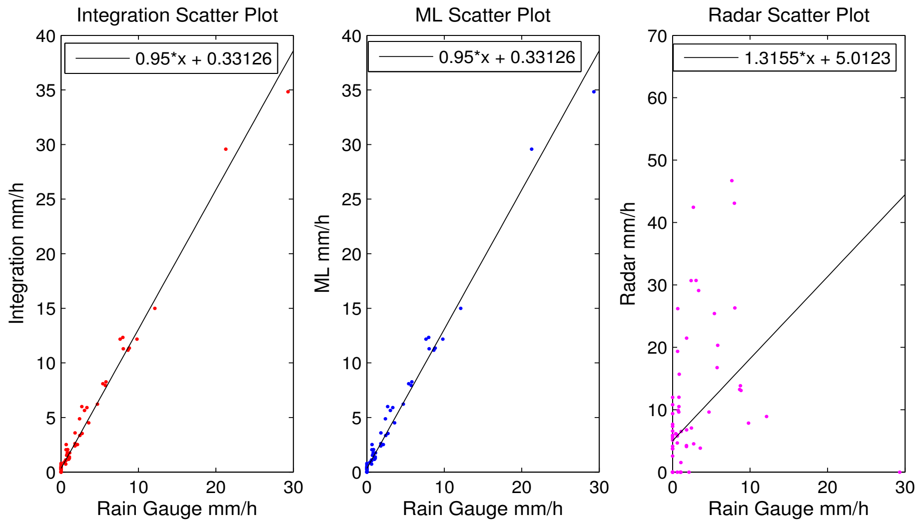


**Fig. 14.** Rain rates scatter plots of the integration (left), the ML (middle) and the radar (right) with respect to the rain gauge in Ramle site for event (1).





AMTD
7, 4481–4528, 2014

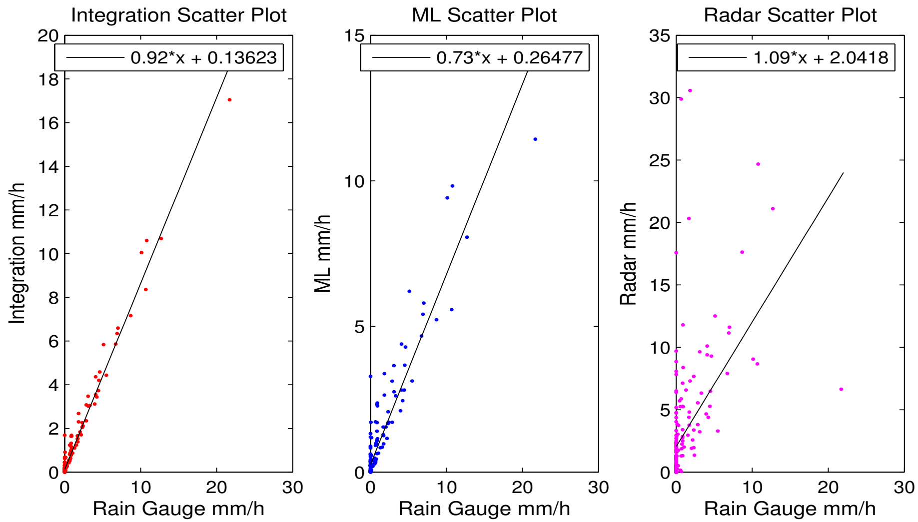


**Fig. 15.** Rain rates scatter plots of the integration (left), the ML (middle) and the radar (right) with respect to the rain gauge in Dorot site for event (2).





AMTD
7, 4481–4528, 2014

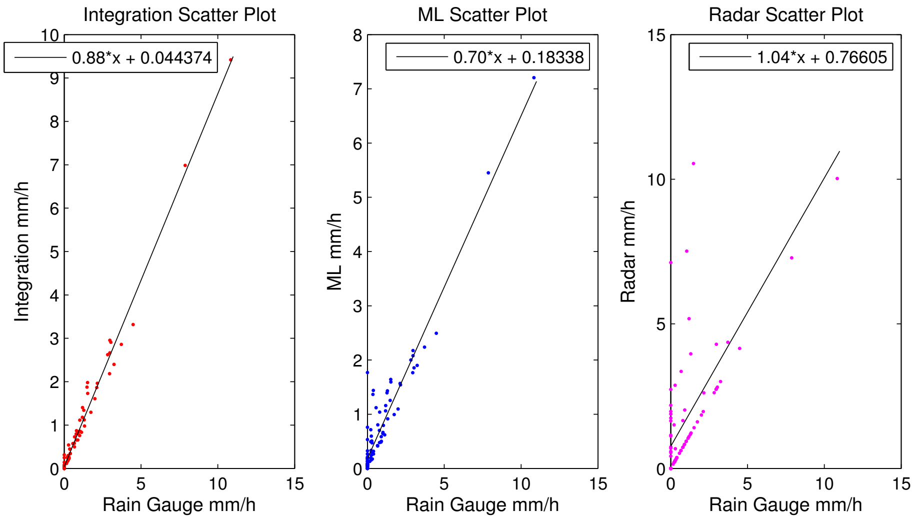


**Fig. 16.** Rain rates scatter plots of the integration (left), the ML (middle) and the radar (right) with respect to the rain gauge in Dorot site for event (3).



AMTD
7, 4481–4528, 2014

Integration between WSN and radar for improved rainfall mapping

Y. Liberman et al.

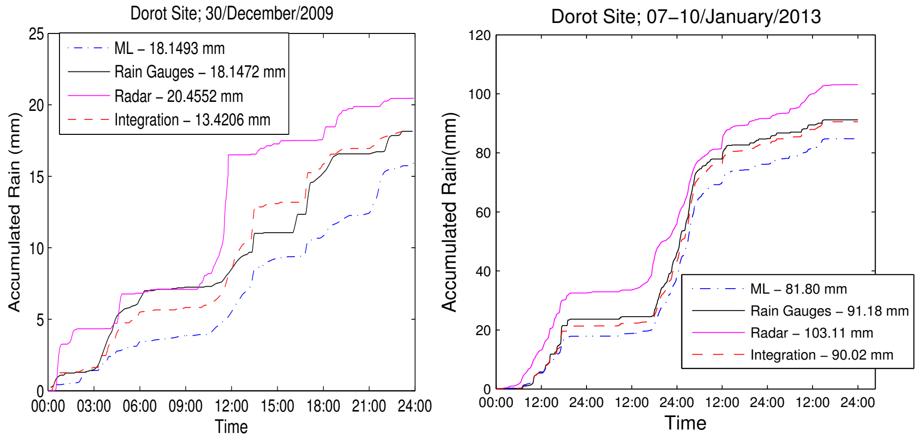


**Fig. 17.** The accumulated rain intensity (mm) for Dorot site, with 12 ML surrounding the site. Left: 30 December 2009 (24 h of rain event), right: 7–10 January 2013 (96 h of rain event).



Discussion Paper | Discussion Paper | Discussion Paper | Discussion Paper |

AMTD

7, 4481–4528, 2014

Integration between WSN and radar for improved rainfall mapping

Y. Liberman et al.

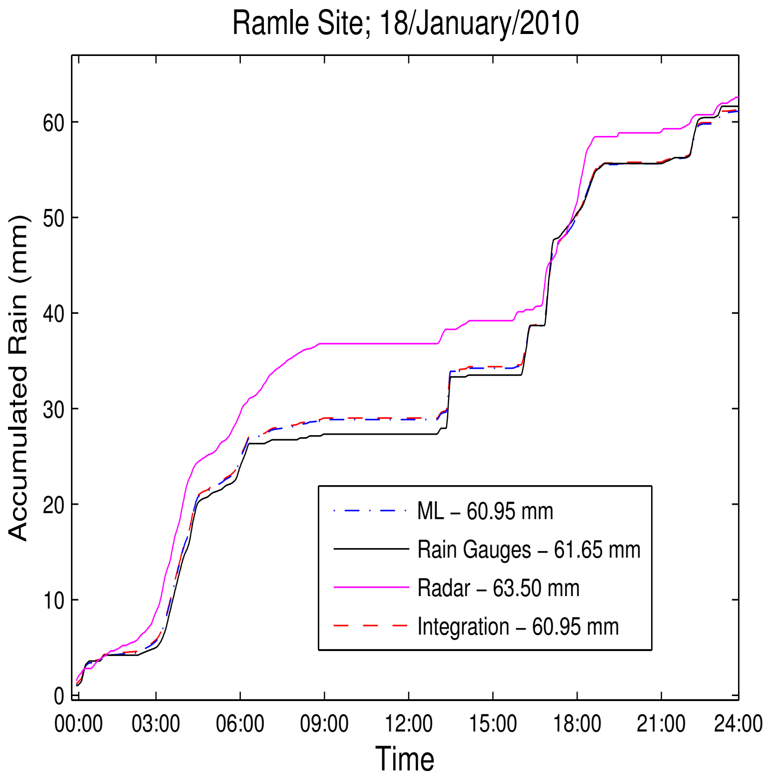


**Fig. 18.** The accumulated rain intensity (mm) for Ramle site, with 30 ML surrounding the site at 18 January 2013 (24 h of rain event).